Ultrathin Nanotube/Nanowire Electrodes by Spin–Spray Layer-by-Layer Assembly: A Concept for Transparent Energy Storage

Forrest S. Gittleson,[†] Daniel Hwang,[†] Won-Hee Ryu,[†] Sara M. Hashmi,[†] Jonathan Hwang,[†,‡] Tenghooi Goh,[†] and André D. Taylor*[,†]

[†]Department of Chemical and Environmental Engineering, Yale University, 9 Hillhouse Avenue, New Haven, Connecticut 06520, United States and [‡]Department of Materials Science and Engineering, Massachusetts Institute of Technology, 77 Massachusetts Avenue, Cambridge, Massachusetts 02139, United States

ABSTRACT Fully integrated transparent devices require versatile architectures for energy storage, yet typical battery electrodes are thick (20–100 μm) and composed of optically absorbent materials. Reducing the length scale of active materials, assembling them with a controllable method and minimizing electrode thickness should bring transparent batteries closer to reality. In this work, the rapid and controllable spin–spray layer-by-layer (SSLbL) method is used to generate high quality networks of 1D nanomaterials: single-walled carbon nanotubes (SWNT) and vanadium pentoxide (V_2O_5) nanowires for anode and cathode electrodes, respectively. These ultrathin films, deposited with ~2 nm/bilayer precision are transparent when deposited on a transparent substrate (>87% transmittance) and electrochemically active in Li-ion cells. SSLbL-assembled ultrathin SWNT anodes and V_2O_5 cathodes exhibit reversible lithiation capacities of 23 and 7 μAh/cm^2, respectively at a current density of 5 μA/cm^2. When these electrodes are combined in a full cell, they retain ~5 μAh/cm^2 capacity over 100 cycles, equivalent to the prelithiation capacity of the limiting V_2O_5 cathode. The SSLbL technique employed here to generate functional thin films is uniquely suited to the generation of transparent electrodes and offers a compelling path to realize the potential of fully integrated transparent devices.

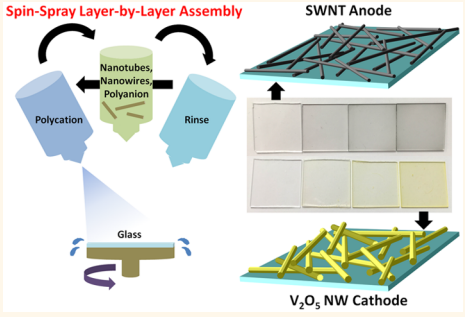

KEYWORDS: multilayer · carbon nanotube · vanadium pentoxide · lithium-ion battery · translucent

Energy storage presents a challenge to the development of seamlessly integrated technologies like wearable devices and transparent displays. Recent enthusiasm for such devices has resulted in robustly flexible and translucent electronics,[1,2] yet energy storage modules to power them remain bulky and difficult to integrate. Improving the versatility of battery design is essential to these applications. Transparency presents a particular challenge, since typical battery electrodes prepared by slurry-based processes are thick (20–100 μm)[3−5] and optically absorbent. Despite the potential to integrate "invisible" energy storage on windows, screens and glasses, there is only one example to date of a transparent battery.[6] While examples of transparent capacitors abound,[7−10] developing batteries with 1–2 orders of magnitude higher energy densities is desirable. The single transparent battery concept reported in literature employed a microfluidic assembly process with careful overlaying of microgrid electrodes.[6] Though 57% transmittance was achieved for a full cell (enough for semitransparency in the visible regime), the microfluidic assembly method in this study is limiting to further applications and inherently unscalable. Here we demonstrate a facile concept for transparent energy storage devices though the precise, bottom-up layer-by-layer deposition of 1D nanomaterials (*i.e.*, nanotubes, nanowires).

Layer-by-layer (LbL) assembly[11−14] is a well controlled, solution-based deposition method applicable in the development of functional thin films, membranes and stackable 2D structures. It uses the electrostatic interaction between two species to generate thin films in a spontaneous yet self-limiting fashion. To date, LbL techniques have been

* Address correspondence to andre.taylor@yale.edu.

Received for review June 12, 2015 and accepted September 7, 2015.

Published online September 07, 2015
10.1021/acsnano.5b03578

used to generate electrochemical components for devices as varied as batteries,[15−19] supercapacitors,[20−25] fuel cells,[26−31] solar cells,[32−34] and sensors.[35−37] Few of these reports, however, justify using the LbL method for its main benefit: nanometer-level precision. While LbL assembly has previously been employed to make battery electrodes up to 18 μm thick,[22] this technique is neither simpler nor more versatile than the commercially prevalent slurry-based method. Where LbL assembly excels is in generating ultrathin (<1 μm) electrodes for potential flexible and translucent devices.

To facilitate LbL deposition for these targeted applications, we previously demonstrated a rapid LbL process called spin−spray layer-by-layer (SSLbL) assembly.[38] The SSLbL technique (Figure 1) involves alternately spraying polyelectrolyte solutions onto a rotating substrate such that electrostatic interactions and simultaneous drying result in tunable ultrathin films. By controlling the amount of material sprayed and the rotation speed of the substrate, among other variables, SSLbL-assembled films can be optimized to yield superior uniformity and functional characteristics (*i.e.*, conductance, transmittance) versus traditional dip-coated LbL films. With sub-nanometer deposition control, the SSLbL technique is a viable "atoms to product" assembly platform for the production of functional ultrathin electrodes.

Though LbL assembly has been repeatedly cited for potential electrochemical applications,[39] its adoption has lagged due to difficulties in discovering and depositing functional materials. LbL deposition of these materials is limited mainly by poor dispersibility and stability in precursor solutions. Despite these challenges, several reports have shown success depositing from colloidal suspensions. Functionalized multi-walled carbon nanotubes (MWNT), for example, can be solubilized and deposited with the LbL method to form binderless supercapacitive electrodes.[20−24] Li-ion battery cathodes with polyaniline (PANI) and sol−gel V_2O_5[16,40,41] or anodes with MWNT and TiO_2[17,42] have also been deposited by various LbL techniques. In these examples, a conductive component (*i.e.*, PANI or MWNT) is used alongside an active component (*i.e.*, V_2O_5, TiO_2) to provide facile electron transport. The choice of active material is largely arbitrary, but nanoscale morphologies are necessary for dispersion and deposition. Functional 1D nanomaterials may address the challenges of resistance and dispersion where other studies have failed. Nanotube and nanowire structures provide large hydrophilic surface areas which promote dispersion and may form 2D networks when deposited on smooth substrates. These 2D networks are conductive when conductive materials are used and exhibit a high void fraction which makes them ideal as transparent electrodes.

In this study, ultrathin and translucent SSLbL-assembled Li-ion electrodes are generated with 1D functional nanomaterials. Single-walled carbon nanotubes (SWNT) and V_2O_5 nanowires are used as the anode and cathode, respectively. SSLbL-assembled electrodes are evaluated for optical transmittance, electrical conductance and electrochemical activity, demonstrating their potential use in transparent energy storage devices. A full Li-ion cell with SSLbL-assembled anode and cathode is also demonstrated to show the applicability of this concept. In their current infancy, transparent battery architectures like those presented here will be most useful in low energy applications (*i.e.*, trickle charging, remote sensing, Bluetooth low energy) or where large surface areas are available (*i.e.*, "smart glass"). The SSLbL process, however, shows significant promise as a tool to improve ultrathin battery design and performance through precise nanomaterial deposition.

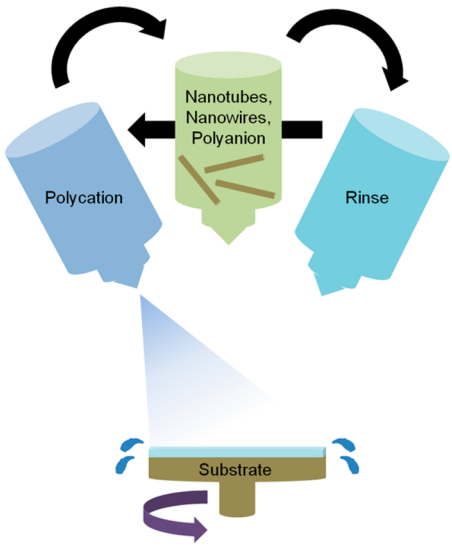

Figure 1. Schematic of the spin−spray layer-by-layer (SSLbL) process for the deposition of 1D nanomaterials.

RESULTS AND DISCUSSION

SWNT Anode Networks. To achieve a transparent energy storage device, the rational selection and careful arrangement of electrode materials is key. Ultrathin, translucent battery electrodes require high capacity, conductive materials to compensate for low loadings, and 2D formations that do not fully block light transmission. With these criteria, 1D anode and cathode nanomaterials were chosen, assembled in ultrathin films with the SSLbL method, and evaluated in half-cell and full cell Li-ion architectures.

We selected SWNT as a viable anode material for this study based on its high theoretical lithiation capacity at 0−1.5 V (~1100 mAh/g)[43−48] and its ability to form conductive and transparent networks.[31,38,46,49−51] Functionalized MWNT has been used previously in LbL-assembled supercapacitors, but this is better suited as a cathode material (at 1.5−4.5 V *vs* Li/Li^+).[21] Pristine MWNT has been used in traditional Li-ion anodes (<1 V *vs* Li/Li^+),

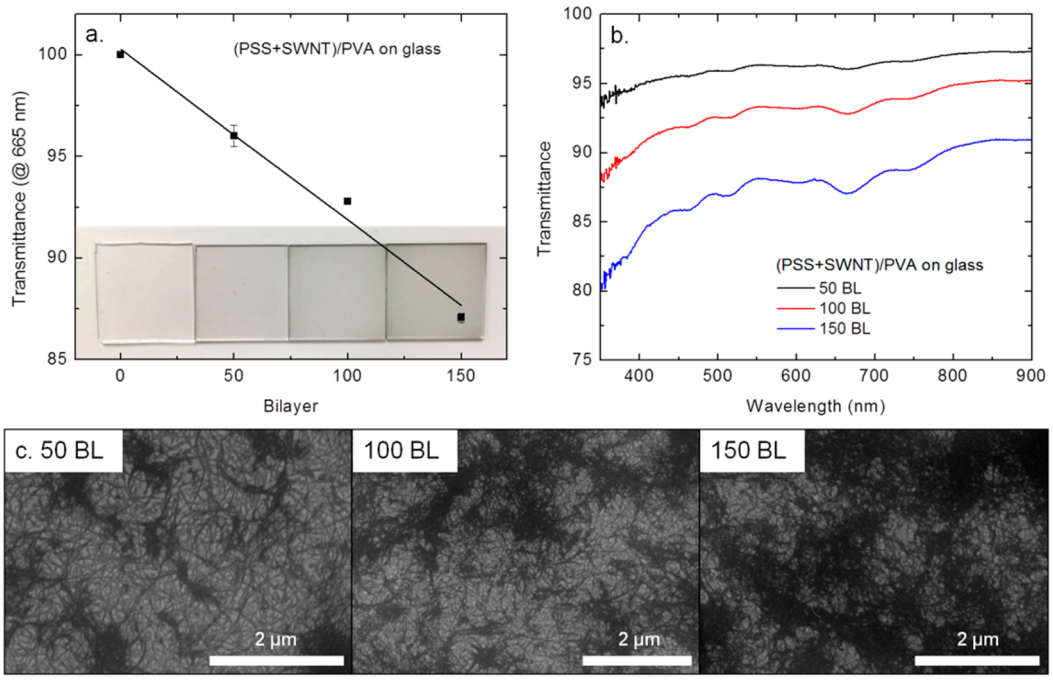

Figure 2. (a,b) Transmittance of (PSS+SWNT)/PVA films on glass and (c) SEM images of the same showing the formation of a percolating conductive network.

but exhibits lower practical capacity (200−300 mAh/g) than SWNT[43] and has a larger diameter (>8 nm *vs* ∼1 nm) which is less conducive to network transparency.

SWNT anode films were deposited by SSLbL assembly from aqueous solutions of 1 wt % poly(styrene sulfonate) (PSS) with 0.5 mg/mL SWNT and 10 mM poly(vinyl acetate) (PVA). (PSS+SWNT)/PVA films were assembled on glass substrates, and their transparency was characterized using UV−vis spectrophotometry. We show that film transmittance at 665 nm exhibits a linear trend with film growth ranging from 96% for 50 BL to 87% for 150 BL (−0.08%/bilayer) (Figure 2a). Since PSS/PVA absorbance is negligible, the decrease in transmittance can be directly attributed to an increasing amount of SWNT deposited.[38] The transmittance spectra of (PSS+SWNT)/PVA films (Figure 2b) are relatively flat across the visible region, with a few features specifically denoting SWNT (*e.g.*, at 665 nm for the (7,6) chirality). The precise and simple tuning of transmittance shown here is a benefit unique to the SSLbL method and supports its application in generating transparent electrodes.

We highlight SEM images of (PSS+SWNT)/PVA film surfaces that show the growth of percolating conductive networks (Figure 2c) and a Raman spectrum that confirms the signature G-band, D-band and RBM region of SWNT (Figure S1 in the Supporting Information). Consistent with our previous modeling study of SSLbL-assembled SWNT films,[49] percolation occurs as the amount of SWNT increases along with the number of SWNT−SWNT junctions. The conductive network formed by this process is essential for the facile transport of electrons to and from reaction sites during Li-ion charging and discharging.

Because of the high sheet resistance of (PSS+SWNT)/PVA films without a current collector (10−1000 kΩ/sq), glass substrates were deemed unsuitable for electrochemical evaluation. Instead, films were deposited on one side of a Celgard separator (Figure S2) and contacted with a stainless steel current collector in half-cells *vs* Li/Li^+. While Celgard is not a transparent substrate, it was chosen rather than ITO-coated glass (common with LbL deposition) due to the poor cycle stability of ITO in the anode potential regime (Figure S3). During cycling below 1 V *vs* Li/Li^+, ITO undergoes an irreversible conversion reaction which generates indium metal and lithium oxide (along with some reversible tin oxide), reducing its conductivity and optical transmittance.[52] While other transparent current collectors exist,[53] few are stable at the extreme potentials required for Li-ion cycling.[54] Those that are stable (*i.e.*, Au, Pt) require nanostructured arrangements that are challenging to implement. In the absence of a reliable, stable and transparent current collector, the electrochemical evaluation of (PSS+SWNT)/PVA films was conducted in non-transparent cells.

We show an SEM image of a typical anode on Celgard (Figure 3a) with some surface roughness due to the porosity and roughness of the underlying substrate. We estimate a 300 BL (PSS+SWNT)/PVA film to be 500−600 nm thick or 1.7−2.0 nm/bilayer. This approximation represents a top range value that can be contrasted with the 0.8 nm/bilayer growth rate we previously observed for (PSS+SWNT)/PVA on smooth

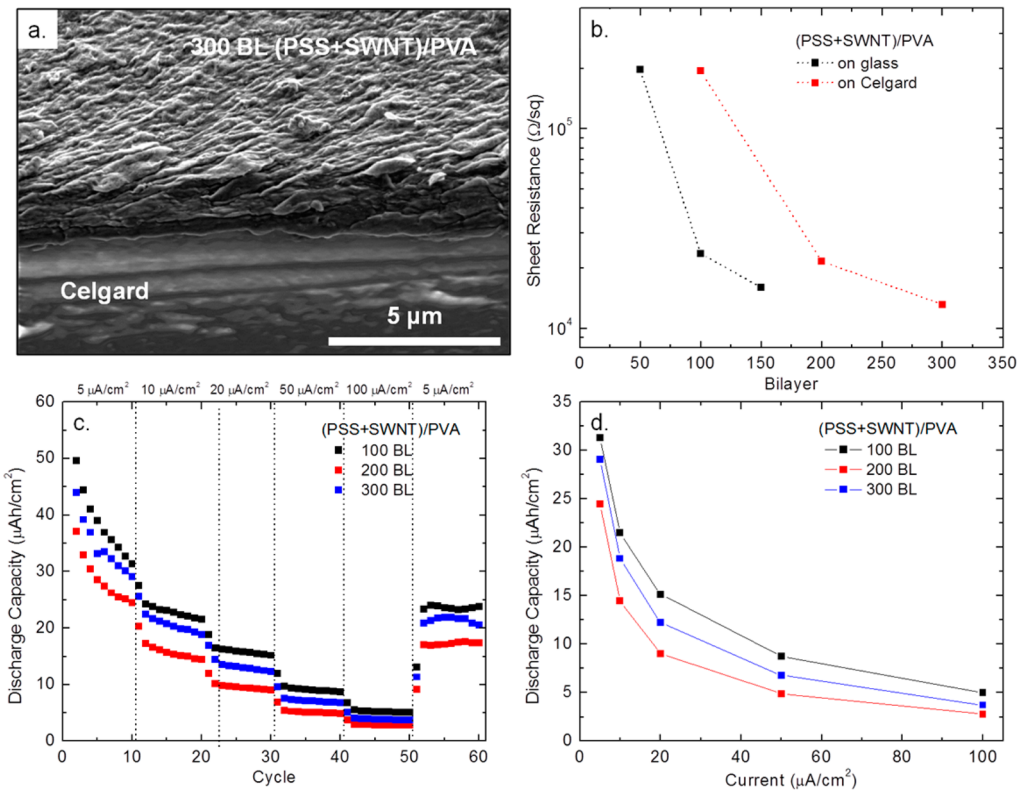

Figure 3. (a) SEM image of a representative (PSS+SWNT)/PVA anode film deposited on a Celgard separator, (b) sheet resistance of (PSS+SWNT)/PVA films deposited on glass and Celgard separators, (c) multi-rate cycling of (PSS+SWNT)/PVA anodes on Celgard *vs* Li/Li$^+$ and (d) current rate *vs* discharge capacity for the same.

Si wafers in thinner samples (<30 BL).[38] In this instance, the increased roughness of the Celgard substrate may yield less compact SSLbL films than those on glass.

The sheet resistances of several (PSS+SWNT)/PVA films on glass and Celgard substrates were compared to elucidate the effect of the substrate on film structure and functional properties (Figure 3b). Electrode resistance in ultrathin films is a major source of ohmic losses and should be minimized as much as possible for practical application. We find that films deposited on Celgard are less conductive per bilayer than those on glass. As noted above, the roughness of Celgard likely plays a role in disrupting the formation of compact conductive networks. To reduce the impact of electrode resistance, electrochemical evaluations were conducted with 100, 200, and 300 BL (PSS+SWNT)/PVA films on Celgard which have roughly similar sheet resistances (10−200 kΩ/sq) as 50, 100, and 150 BL (PSS+SWNT)/PVA films on glass. Since the structure of films on glass and Celgard are clearly different, we accept that comparisons between transmittance and electrochemical properties are imperfect. For this reason, we also overlook the obvious difference in active material loadings between the two sample groups.

(PSS+SWNT)/PVA anode films on Celgard were evaluated by galvanostatic lithiation and delithiation at 0−1.5 V *vs* Li/Li$^+$ over several current densities. We present the average discharge capacity of 3 cells for each sample (Figure 3c). Though all SSLbL anodes undergo some degradation in discharge capacity during the first several cycles due to passivation, they are more stable at higher current rates and in later cycles. We expect that this passivation reaction involves the formation of a solid electrolyte interface (SEI) by electrolyte decomposition, typical in Li-ion batteries.[55] The large electrochemical surface area provided by SWNT, compared to traditional graphitic anodes, is a likely source of this irreversible capacity (~120 μAh/cm^2 during the first discharge), but one that cannot be avoided with high aspect ratio 1D nanomaterials. We find that reversible discharge capacity after 60 cycles is greatest for the thinnest 100 BL anode (~23 μAh/cm^2 at 5 μA/cm^2), which we attribute to improved electrical contact between the stainless steel current collector and active material. 200 and 300 BL electrodes exhibit discharge capacities of 17 and 21 μAh/cm^2, respectively, at 5 μA/cm^2. A graph complete with error bars representing the standard deviation of these values (Figure S4), however, shows that differences in capacity between the 100, 200, and 300 BL films may not be statistically significant. Accepting that the SWNT loading increases in proportion to the number of bilayers, it is interesting to note that higher loadings do not yield greater capacities. A likely explanation is the encapsulation of active material in the insulating PSS/PVA polymer matrix, which leaves only those materials

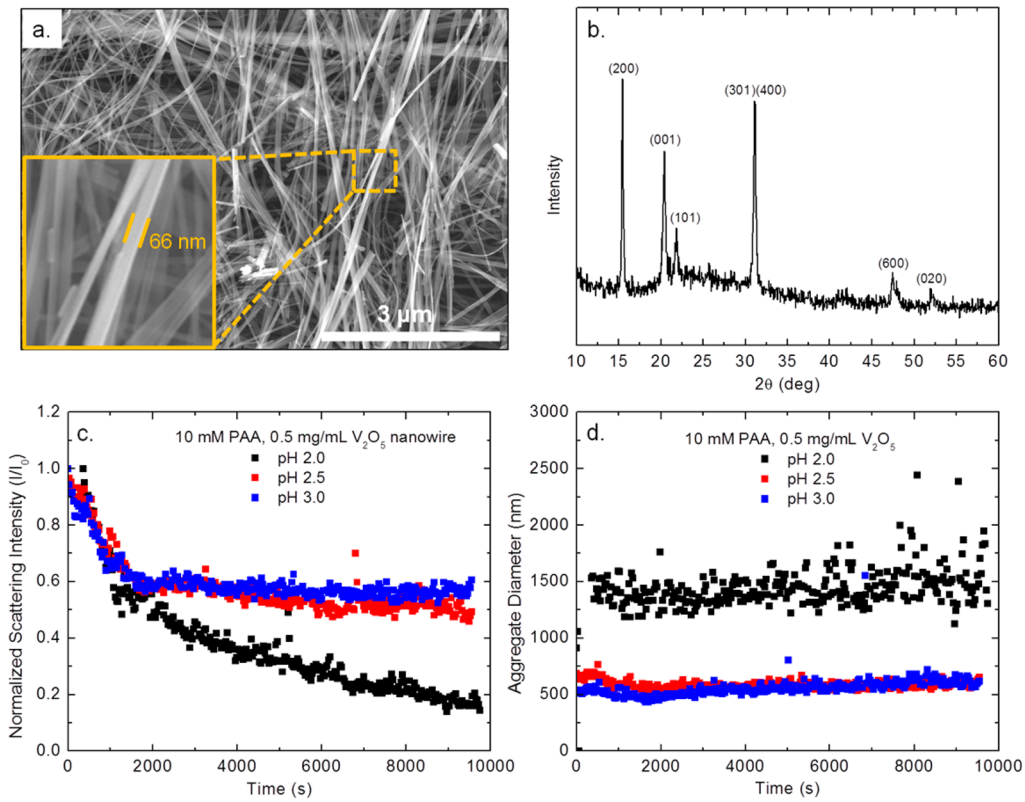

Figure 4. (a) Morphology of hydrothermally synthesized V_2O_5 nanowires and (b) XRD of the same. Dynamic light scattering (c) normalized intensity and (d) aggregate size for 10 mM PAA solutions with 0.5 mg/mL V_2O_5 nanowires.

at the current collector interface accessible to Li^+ binding.

We also provide a summary of discharge capacity versus current rate for SWNT anodes (Figure 3d). The reduction in capacity at greater current rates for all electrodes is an indicator that lithiation is hindered by poor ion diffusion and lower than ideal electrical conductance in SWNT networks. These results again suggest functional limitations to SWNT-composite anodes stemming from polymer encapsulation. To improve rate capability and cycle performance, reducing polymer concentrations is desirable in future studies. Doping SWNT films to enhance electrical conductivity[56] or employing electroactive polymers (with optical transparency) may also benefit electrode function without sacrificing the advantages of the SSLbL-assembly process. With such advances, SSLbL-assembled SWNT electrodes can be further optimized in capacity and rate capability. Nevertheless, SSLbL-assembled SWNT networks present a compelling concept for conductive, transparent battery anodes.

V_2O_5 Nanowire Cathode Networks. We selected vanadium pentoxide as a viable cathode material for this study as it exhibits one of the highest theoretical energy densities among next-generation Li-ion cathodes (274 mAh/g for $Li_2V_2O_5$). During lithiation, orthorhombic V_2O_5 transitions through several phases corresponding to α-V_2O_5 → ε-$Li_{0.5}V_2O_5$ → δ-$Li_1V_2O_5$ → γ-$Li_2V_2O_5$ → ω-$Li_3V_2O_5$, but only up to γ-$Li_2V_2O_5$ (achieved at ~2.2 V *vs* Li/Li^+) is fully reversible without a change in structure[57] (Figure S5). To promote the rapid insertion (and removal) of Li^+ in orthorhombic V_2O_5 and thereby reduce ohmic losses, we selected high aspect ratio nanowire morphologies for this study.[58−61] V_2O_5 nanowires also adopt negative surface charges in pH adjusted aqueous solutions,[62,63] aiding dispersion and making them ideal for SSLbL-assembly of ultrathin, transparent network cathodes.

V_2O_5 nanowires were synthesized with a facile, bulk hydrothermal method previously reported by our group.[64] The aspect ratio of synthesized V_2O_5 nanowires is >150 with a bundle diameter of ~66 nm (Figure 4a). We show that the X-ray diffraction pattern (Figure 4b) and Raman spectrum (Figure S6) of this material are in line with the crystallinity (JCPDS card 41−1426) and bonding of orthorhombic V_2O_5 with no impurity phases.[65−67]

For SSLbL deposition, V_2O_5 nanowires were dispersed in polyanionic solutions of poly(acrylic acid) (PAA) and deposited with polycationic solutions of poly(ethylene oxide) (PEO) with lithium triflate (LiTrif). We note that PAA has been used before as a binder material in Li-ion electrodes[68] and was employed in several studies to generate polymer electrolyte films with PEO by traditional dip-coating LbL-assembly.[69,70] Lithium triflate was incorporated into PEO solutions to improve the ionic conductivity of the resulting films.[71]

Achieving dispersion stability of colloidal particles is essential in spray-based LbL-assembly to achieve

uniform films and prevent sprayer clogging. While dispersing SWNT for anode films is relatively easy with the use of PSS, we employ dynamic light scattering experiments to evaluate the stability of V_2O_5 nanowires in PAA solutions of varying concentration and pH. We provide the normalized scattering intensity (I/I_0) of V_2O_5 nanowires in 10 mM PAA solutions from pH 2.0 to 3.0 (Figure 4c) and the aggregate particle size of the same, using a spherical aggregate assumption (Figure 4d). We observe that all suspensions undergo rapid settling during the first ~20 min due to an effect of diluting the V_2O_5 stock dispersion immediately before the measurement. After the initial settling, the behavior of I/I_0 indicates longer-term stability. Solutions of pH 2.5 and 3.0 produce more stable V_2O_5 nanowire dispersions (slower settling) than pH 2.0, but there is little difference in stability or aggregate particle size between pH 2.5 and 3.0. The continued settling of the suspension at pH 2.0 results from larger aggregate sizes (Figure 4d). We conclude that pH affects the density of charges on V_2O_5 nanowire surfaces such that nanowires are more repellent to each other at pH 2.5 or 3.0 than at pH 2.0. This agrees with a previous report stating that V_2O_5 nanoribbons are better stabilized close to pH 2.6.[72]

We also evaluated the effect of PAA concentration on V_2O_5 dispersion stability by light scattering, with the normalized scattering intensity and aggregate diameter results provided in Tables 1 and 2, respectively. While there is a benefit to having some PAA in solution (at least 5 mM), there is little difference between the stability of 5, 10, and 20 mM PAA dispersions after 2.5 h. In general, smaller aggregate sizes with PAA correspond to higher values of I/I_0, indicating increased suspension stability. We conclude that PAA has minimal coordination with the V_2O_5 nanowire surface beyond acting as a surfactant at very low concentrations (<5 mM). Repellent negative surface charges on PAA and V_2O_5 around pH 2.5 therefore suggest LbL-assembly of PAA/PEO and V_2O_5/PEO are separate adsorption processes occurring simultaneously but resulting in the desired film structure. Dynamic light scattering thus provides a useful tool for understanding the LbL-assembly process and optimizing nanoparticle dispersion stability. Using these results, we selected a standard concentration of 10 mM PAA at pH 2.5 for SSLbL deposition of V_2O_5 nanowires.

(PAA+V_2O_5)/(PEO+LiTrif) films were deposited by SSLbL-assembly on glass substrates to evaluate their optical transmittance. Transmittance values for these films range from 96% for 50 BL to 87% for 150 BL. We show the linear correlation of transmittance per bilayer at 665 nm (−0.08%/bilayer), similar to that of SWNT-containing films (Figure 5a). Transmittance spectra for these films (Figure 5b) shows a single distinguishing feature at 413 nm related to V^{5+}, consistent with a V_2O_5 stoichiometry. The transmittance of PAA/(PEO+LiTrif) films generated with the same settings but without V_2O_5 nanowires are provided for comparison (Figure S7). We find that only ~10% of the decrease in transmittance is due to the polymer matrix for this system and the remainder is due to V_2O_5 nanowire deposition. Rinse time during SSLbL-assembly was also varied from 0.2 to 0.5 s to control the amount of V_2O_5 (Figure S8). We find that a minimal rinse step (0.2 s) is necessary to achieve film uniformity without removing too much active material. Dip-coating LbL-assembly, with lengthy rinse steps, is therefore unsuitable for V_2O_5 nanowire deposition and the SSLbL technique, with reduced residence times, is needed. SEM images of SSLbL-assembled (PAA+V_2O_5)/(PEO+LiTrif) films (Figure 5c) confirm a good dispersion of V_2O_5 nanowires and the formation of 2D networks which supports their application in transparent electrodes.

TABLE 1. Normalized Light Scattering Intensity (I/I_0) after 2.5 h[a]

PAA concentration (mM)	pH 2.0	pH 2.5	pH 3.0
0	0.14 ± 0.03	0.46 ± 0.03	0.20 ± 0.02
5	—	0.53 ± 0.02	—
10	0.17 ± 0.01	0.50 ± 0.02	0.57 ± 0.02
20	0.13 ± 0.02	0.5 ± 0.1	—

[a] Higher value indicates greater dispersion stability.

TABLE 2. V_2O_5 Aggregate Diameter (nm) in Solution after 2.5 h, Assuming Spherical Aggregates

PAA concentration (mM)	pH 2.0	pH 2.5	pH 3.0
0	13110 ± 29000	1200 ± 80	2920 ± 720
5	—	860 ± 40	—
10	1520 ± 190	610 ± 30	600 ± 30
20	1210 ± 280	820 ± 430	—

Despite a decent conductivity of ~0.5 S/cm for a single V_2O_5 nanowire, nanowire networks of this material generally exhibit poor conductances.[73] Previous examples of LbL-assembled cathodes have combined sol−gel V_2O_5 with polyaniline[16,40,41] to improve electrode conductivity, but polyaniline is optically absorbent and therefore unsuitable for transparent electrode applications. To improve the electrical conductance of V_2O_5 nanowire films, we devised an architecture in which SWNT-containing layers were integrated above and below V_2O_5-containing layers. A schematic of this "sandwich" structure is provided in Figure 6a and represents the first example of two different LbL-assembled films being deposited in a bottom-up fashion. For comparison, the optical transmittance of SWNT-V_2O_5-SWNT sandwich structures on glass demonstrates a linear correlation with (PAA+V_2O_5)/(PEO+LiTrif) film growth (−0.08%/bilayer), equivalent to those films without SWNT (Figure S9). The addition of 100 bilayer (PSS+SWNT)/PVA films on each side of the V_2O_5 active layer results in a transmittance penalty of −12%, but

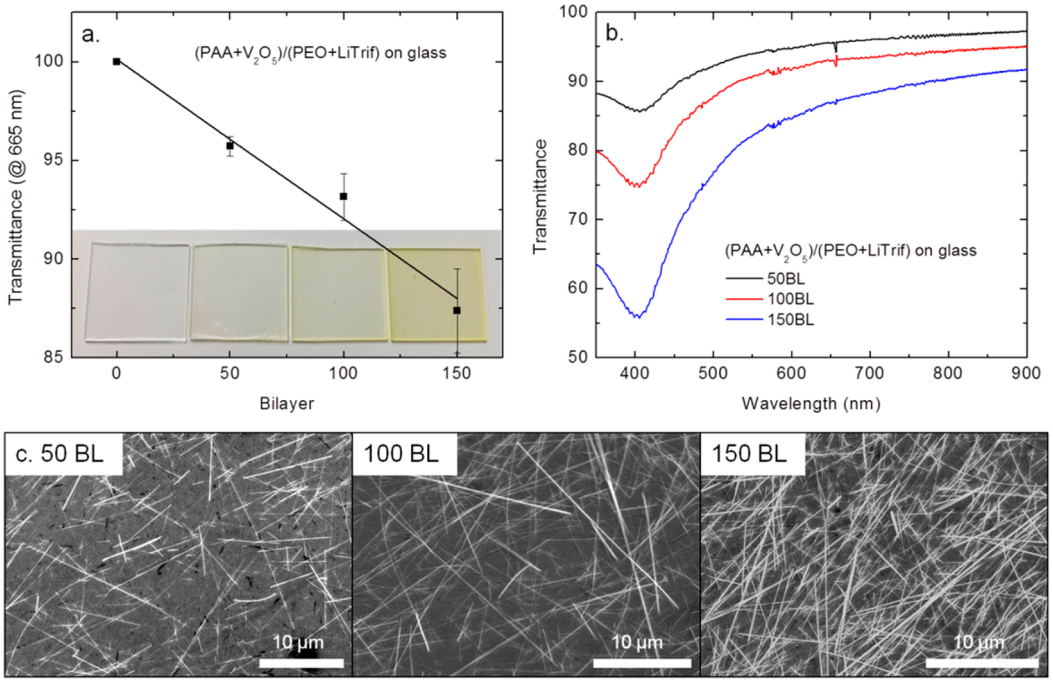

Figure 5. (a,b) Transmittance of (PAA+V_2O_5)/(PEO+LiTrif) films on glass and (c) SEM images of the same.

electrodes still exhibit >75% transmittance. The multilayered sandwich architecture presented here is widely applicable beyond the transparent electrodes in this work and should encourage LbL-assembly in a variety of integrated devices.

For electrochemical evaluation (PAA+V_2O_5)/(PEO+LiTrif) sandwich cathode films were deposited *via* SSLbL-assembly on Celgard separators and contacted with stainless steel current collectors. Despite the stability of ITO in the cathode potential regime, we find that delamination of SSLbL electrodes from glass-based substrates negatively impacts their performance. We show the morphology of a 100 BL (PAA+V_2O_5)/(PEO+LiTrif) sandwich film on Celgard *via* SEM (Figure 6b). While film wrinkles at the edge are a result of electrode cutting, high aspect ratio, rigid V_2O_5 nanowires and "wavy" SWNT are evident. The thickness of this 100 BL (PAA+V_2O_5)/(PEO+LiTrif) sandwich film is approximately 150−300 nm with a large variation for roughness caused by the underlying substrate and layering of ~66 nm diameter V_2O_5 bundles.

We show the improvement in electrode resistance with the SWNT-V_2O_5-SWNT sandwich structure in Figure 6c: 3−4 orders of magnitude on Celgard and 4−5 orders of magnitude on glass substrates versus the detection limit. As with SWNT anode films, the roughness of Celgard substrates yields higher resistances for sandwich cathodes on Celgard than the same films deposited on glass. We also note that thicker (PAA+V_2O_5)/(PEO+LiTrif) layers produce more resistive sandwich electrodes than thinner layers, likely due to decreased interpenetration between the top and bottom SWNT networks.

We highlight the reversible cycling of V_2O_5 sandwich cathodes on Celgard at a range of current densities (Figure 6d,e). Unlike anode films which exhibit significant passivation-related capacity in initial cycles, these ultrathin cathodes are quite stable. We find that the thinnest 50 BL (PAA+V_2O_5)/(PEO+LiTrif) cathode exhibits a higher lithiation capacity (7.0 μAh/cm^2) than the thicker and less conductive 100 and 150 BL cathodes (6.5 and 5.7 μAh/cm^2, respectively) at 5 μA/cm^2. Despite the proportionate increase in V_2O_5 loading in thicker films (apparent from transmittance data), the insulating PAA/PEO polymer matrix likely encapsulates and isolates much of this material so that only the V_2O_5 near the current collector interface is active, similar to SSLbL-assembled SWNT anodes. We also show that the capacities decrease as current densities increase: a result of non-ideal electrical contact between the active material and current collector (Figure 6e). As with SWNT anodes, reducing polymer concentrations and selecting electroactive polymers should improve the capacity of ultrathin V_2O_5 cathodes in future studies.

V_2O_5 sandwich electrodes on Celgard were inspected before and after cycling by SEM to evaluate film stability (Figure S10). Except for some mechanical tearing of films during cell assembly, (PAA+V_2O_5)/(PEO+LiTrif) sandwich cathodes remain fully intact. Remarkably, we notice a distinct color change in V_2O_5-containing films: yellow before lithiation to blue after lithiation. This phenomenon was investigated in 100 BL (PAA+V_2O_5)/(PEO+LiTrif) films deposited on ITO-coated glass by SEM and UV−vis spectrophotometry (Figure S11). Though V_2O_5 nanowires are unchanged in morphology following lithiation, their transmittance at 413 nm is

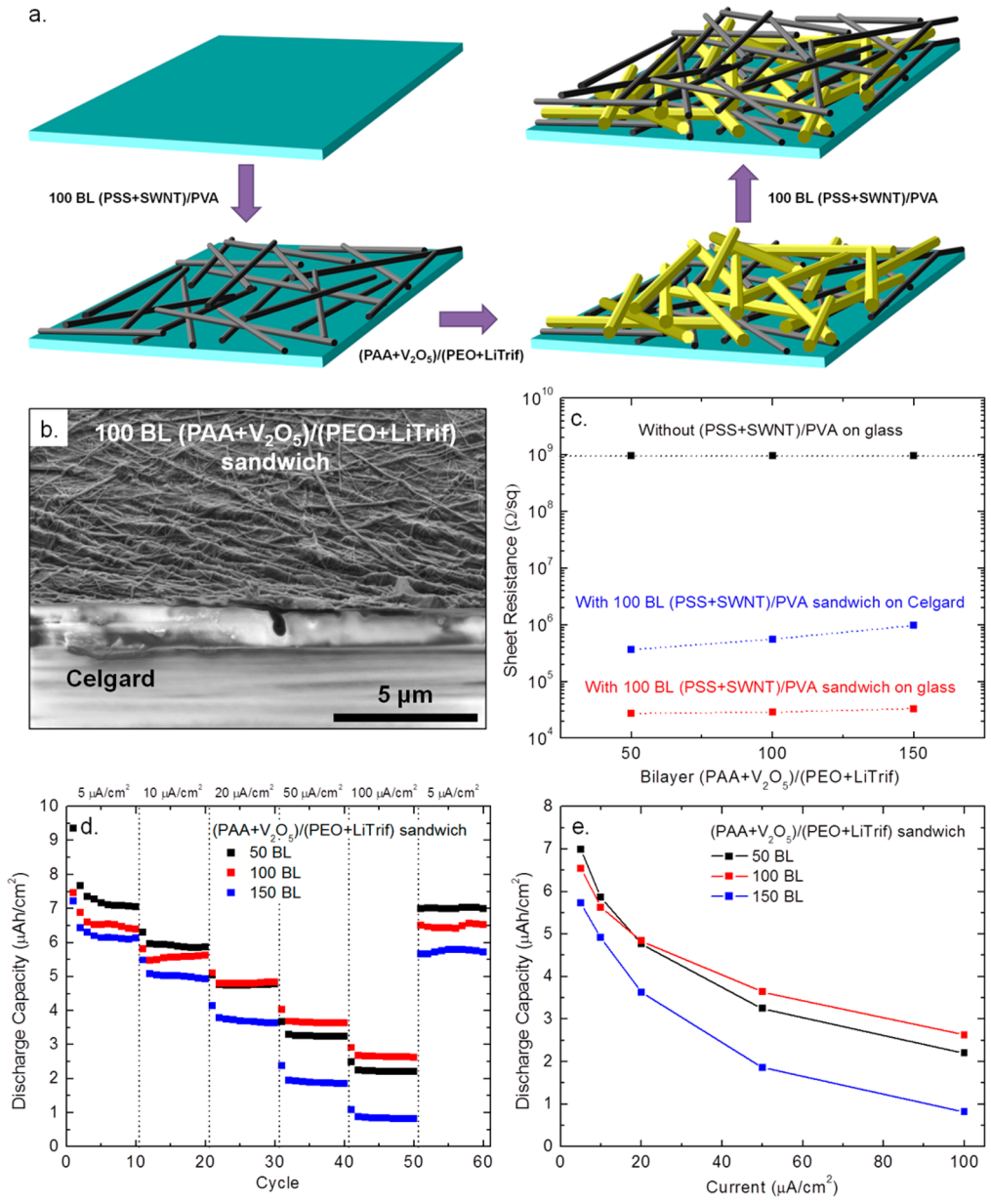

Figure 6. (a) Schematic of (PAA+V_2O_5)/(PEO+LiTrif) cathode layer sandwiched between 100 BL (PSS+SWNT)/PVA layers where black rods represent SWNT and yellow rods represent V_2O_5, (b) SEM image of this structure on a Celgard separator, (c) sheet resistance comparison with and without SWNT layers (black dotted line denotes measurement threshold), (d) multi-rate cycling of (PAA+V_2O_5)/(PEO+LiTrif) sandwich cathodes on Celgard *vs* Li/Li^+ and (e) current rate *vs* discharge capacity for the same.

increased, consistent with a decrease in the amount of V^{5+}. The transition to a blue hue is indicative of V^{4+} formation, likely present in the desired γ-$Li_2V_2O_5$ stoichiometry.[74,75]

Toward a Full Transparent Cell. We provide a comparison of cathode capacity among previous LbL reports to contextualize the benefit of our SSLbL-assembled ultrathin electrodes (Figure 7). We note that the area normalized capacity of LbL-assembled cathode films is directly correlated with electrode thickness for both MWNT-based and PANI/V_2O_5-based electrodes. While our 100 BL V_2O_5 nanowire electrode (~200 nm thick) is consistent with this general trend, it is the only example of a translucent, ultrathin electrode. The closest example, a ~ 300 nm thick, non-transparent MWNT electrode, exhibits a lower capacity (~3.8 *vs* 5.6 μAh/cm^2) in the same voltage range (2−4 V) and at the same current rate (10 μA/cm^2). All other V_2O_5-containing LbL electrodes display lower areal capacities per thickness (at 5 μA/cm^2) than our SSLbL-assembled V_2O_5 nanowire cathode. Despite the obvious trade-off between energy storage capacity and transparency (a function of active material loading, absorbance, nanostructure and arrangement), SSLbL-assembly is ideally suited to improve the performance of ultrathin, transparent electrodes.

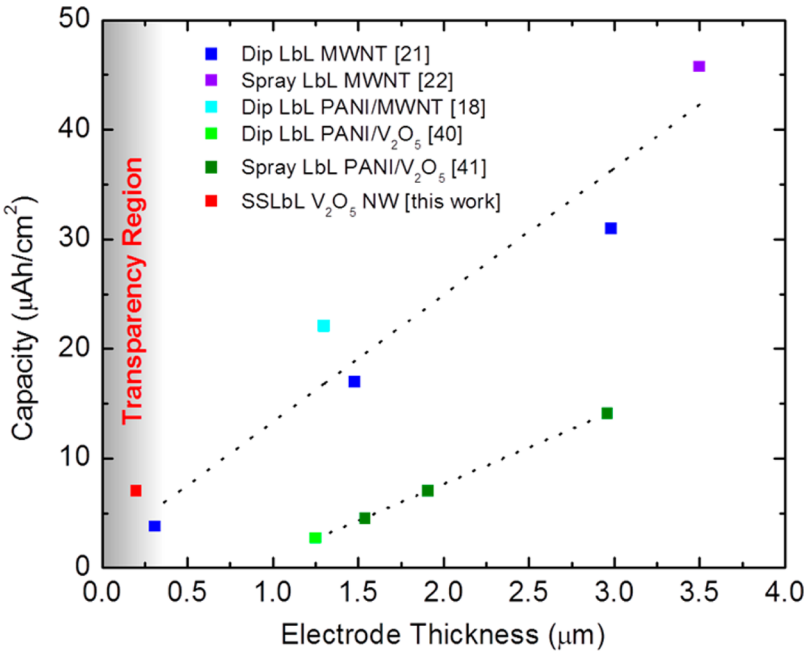

Figure 7. Comparison of LbL-assembled cathodes. Capacity values were derived from cycle profiles in a comparable 2−4 V range at 5 μA/cm^2 or the lowest reported current rate. Dotted lines for MWNT-based and PANI/V_2O_5-based LbL electrodes are guides for the eye. The transparency region will depend on the loading, absorbance, nanostructure and arrangement of materials, in addition to the electrode thickness.

To show the applicability of this process, we combined SSLbL-generated anode and cathode films (on Celgard) in a proof-of-concept full Li-ion cell (Figure 8a). Prior to cell assembly, a 100 BL (PAA+V_2O_5)/(PEO+LiTrif) sandwich cathode was prelithiated to 5 μAh/cm^2 in a half-cell *vs* Li/Li$^+$. Following lithiation, the cathode was placed counter to a 100 BL (PSS+SWNT)/PVA anode with an extra Celgard separator between them to eliminate shorting. Galvanostatic cycling results at 5 μA/cm^2 (~1 C) of a 1 cm^2 full cell architecture are presented in Figure 8b. With the cathode film as the limiting electrode in this cell, a discharge/charge capacity of ~5 μAh/cm^2 is stably maintained over 100 cycles. The initial decrease in capacity over the first 20 cycles is due to passivation of the anode, similar to that seen in half-cells and explained by SEI formation. In spite of losses from the anode, the full cell retains a capacity at 100 cycles, very similar to the initial prelithiation capacity of the V_2O_5 cathode (Figure 8c). The full cell voltage profile is typical of both V_2O_5 and SWNT electrodes, as both exhibit sloping lithiation and delithiation curves (Figure S12). Comparing the voltage response of a full cell to those of half cells, we attribute a ~ 1 V full cell hysteresis primarily to non-ideal anode function. The effect of irreversible capacity and voltage overpotentials in full cells may be reduced in future studies through a combination of aforementioned methods: reducing polymer content, improving electrode conductivity and modifying active material properties.

This concept cell represents the first LbL-assembled full Li-ion battery architecture using anode and cathode intercalation materials. Although lithiation capacities and current densities for this ultrathin cell are not as high as for conventional batteries due to the limited amount of active material, the processes demonstrated here provide a path for future improvements. With the advent of stable, transparent current collectors and the use of a transparent electrolyte, the facile generation of transparent batteries by SSLbL-assembly is possible.

CONCLUSION AND OUTLOOK

Improving the versatility of battery designs is necessary to facilitate transparent devices. In this work, we used the highly controllable SSLbL-assembly technique to generate ultrathin network electrodes from SWNT and V_2O_5 nanowires. Their application as transparent films (>87% transmittance) and electrochemically active electrodes was demonstrated. Combining these two functions in a full transparent battery, however, necessitates (1) a stable, transparent current collector and (2) a transparent electrolyte, the latter being relatively trivial. The design concept for a network electrode of 1D nanomaterials generated by SSLbL-assembly has proven effective, but further optimization, specifically of electrode resistances and active material utilization, should yield improvements to storage capacity and current density. To partially address this, we integrated separate conductive and active LbL-assembled layers in a 2D stack, which is the first of its kind. With this "sandwich" design, conductive layers can be easily incorporated to improve the performance of poorly conductive active materials. Implications of this structure

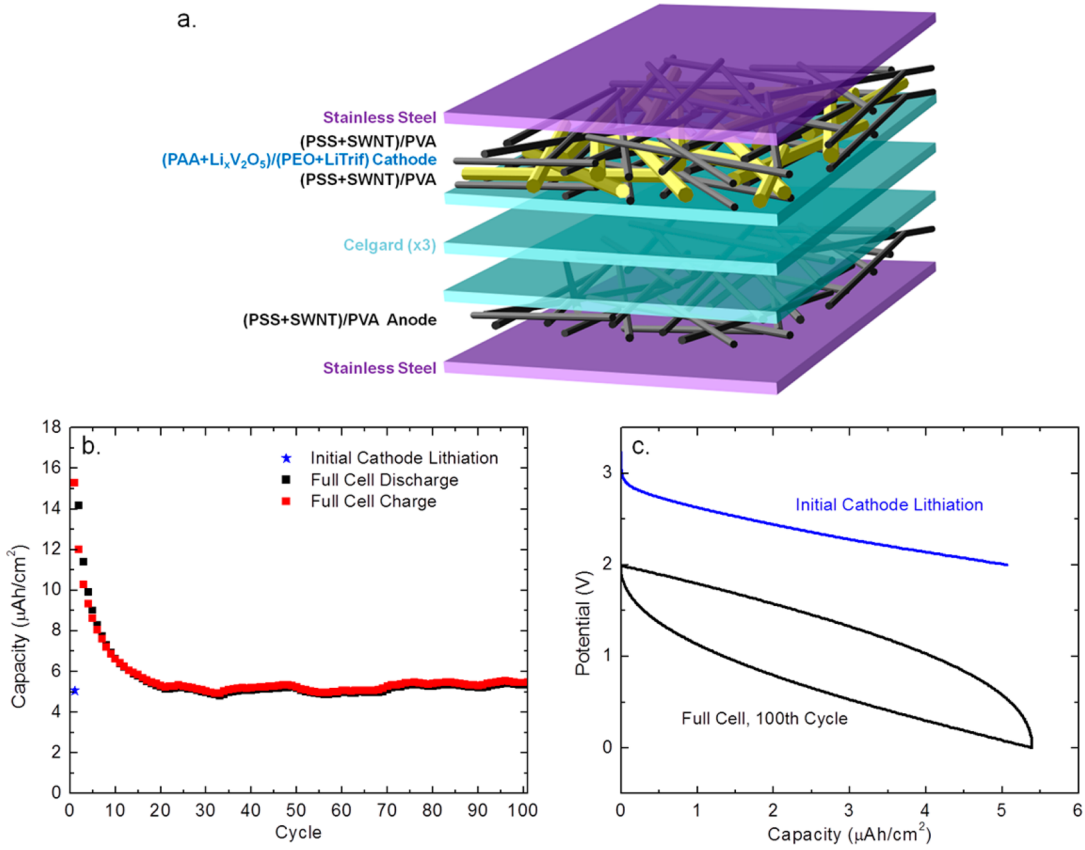

Figure 8. (a) Schematic of full cell battery with SSLbL-assembled SWNT anode and V_2O_5 nanowire cathode, (b) cycling data for full cell over 100 cycles at a rate of 5 μA/cm^2 and (c) cycle profiles of the same (initial cathode lithiation *vs* Li/Li$^+$).

exist beyond transparent battery electrodes in electrochromics, solar cells, sensors and "smart glass" technology. The precise, solution-based and potentially scalable deposition of 1D nanomaterials presented here offers a new paradigm for generating transparent energy storage devices.

METHODS

Materials. Poly(styrene sulfonate) (PSS, MW 1 000 000), and poly(vinyl alcohol) (PVA) were purchased from Sigma-Aldrich. Poly(acrylic acid) (PAA, 25% in H_2O, MW 50 000) and poly-(ethylene oxide) (PEO, MW 4 000 000) were purchased from Polysciences Inc. Bulk vanadium pentoxide was purchased from Sigma-Aldrich. Lithium trifluoromethanesulfonate (LiTrif) was purchased from Alfa Aesar. High purity SWNTs (SG76) were donated by SouthWest NanoTechnologies.

Solution Preparation. All polymers were dissolved or diluted in Milli-Q deionized water. Polyelectrolyte dispersions containing SWNTs were bath sonicated for 6 h and centrifuged at 3000 rpm for 1.5 h to produce a stable dispersion. Typical SWNT dispersions consisted of 0.5 mg/mL SWNT in aqueous solutions of 1 wt % (48.5 mM) PSS. V_2O_5 nanowires were hydrothermally synthesized from bulk V_2O_5 as reported previously.[64] V_2O_5 nanowire dispersions (0.5 mg/mL) in 10 mM PAA solution were produced by tip sonication for 1 h and used immediately after removal of large aggregates by decanting. Ten mM LiTrif was included in PEO solutions. Solution pH was adjusted using HCl and NaOH. Ten mM PAA and PEO solutions were adjusted to pH 2.5 and 10 mM PVA solutions were adjusted to pH 2.8. PSS+SWNT solutions were not pH adjusted.

Dynamic Light Scattering. Stock suspensions of 0.5 mg/mL V_2O_5 nanowires were prepared by probe sonication in pH adjusted aqueous solutions of PAA. These dispersions were diluted 15-fold with the same pH-adjusted solution to a final concentration of ~0.04 mg/mL V_2O_5. Dynamic light scattering measurements were acquired at intervals of 30 s over 2.5 h for each sample, at a fixed angle $\theta = 90°$ using a CGS-5000F goniometer (ALV). The incident laser wavelength was 532 nm (Coherent), yielding the scattering vector $q = (4\pi n_0/\lambda_0) \sin(\theta/2) = 0.022$ nm^{-1}, where n_0 is the index of refraction of the solvent. We assume $n_0 = 1.33$ for water. On-board correlator cards fit the raw data to obtain the diffusive time scale, τ, with the diffusion constant $D = 1/(2q^2\tau)$. We estimate the spherical-equivalent aggregate size, a, using the Stokes–Einstein relation $D = k_BT/6\pi\eta a$, where k_B is the Boltzmann constant, $T = 295$ K, and η is the viscosity of water. In addition to size information, we collect the scattered light intensity I/I_0 as a function of time, where I_0 is the incident intensity, to assess the settling of aggregates in suspension.

SSLbL Assembly. The SSLbL apparatus used for film deposition was the same as described previously.[38] Films were either deposited on glass or ITO-coated glass (cleaned by sonication in ethanol, acetone, and water) with a 3000 rpm spin rate. Substrates for anode and cathode films were heated to ~40 °C during SSLbL deposition using an integrated blown hot air element. Rinse times between polyanion and polycation sprays were 1.0 s for SWNT films and 0.2 s for V_2O_5 films. Spray times were 0.5 s for all polyelectrolyte dispersions and solutions. Electrodes for galvanostatic cycling were deposited on non-transparent Celgard 2325 porous separators (~25 μm thick) stretched on rigid aluminum metal. Film growth for SSLbL-assembly is noted in bilayers (BL), a single deposition cycle of polyanion and polycation.

Optical and Physical Characterization. Transmittance measurements of SSLbL-assembled films on glass were obtained using a Hewlett-Packard UV−vis spectrophotometer. Raman measurements were made with a Jasco 3100 laser Raman spectrophotometer with a 785 nm excitation wavelength. SEM images were obtained using a Hitachi SU-70 scanning electron microscope. X-ray diffraction was conducted with a Bruker D8 Focus X-ray diffractometer.

Electrochemical Evaluation. Anode and cathode half-cells with electrodes deposited on Celgard substrates were assembled in Teflon-lined Swagelok cells with stainless steel current collectors. Electrodes were cut to a geometric surface area of 1 cm^2 and placed face down against the current collector. A second Celgard separator was placed on top followed by a Li foil counter electrode and several drops of 1 M $LiPF_6$ in 1:1 ethylene carbonate/dimethyl carbonate electrolyte. Galvanostatic cycling was conducted with various current rates over 0−1.5 V for the anode and 2.0−4.0 V for the cathode. All electrodes were dried under vacuum and assembled into cells in an argon purged glovebox. Cell cycling was conducted using a Biologic VSP potentiostat.

Conflict of Interest: The authors declare no competing financial interest.

Acknowledgment. The authors gratefully acknowledge Profs. Lisa Pfefferle and Gary Haller for use of the Raman equipment and Prof. Menachem Elimelech for use of the UV−vis spectrophotometer. The National Science Foundation NSF-CBET-0954985 CAREER Award and Teracon Corp. provided partial support of this work. W.-H. R. acknowledges support from The NatureNet Program of the Nature Conservancy. Southwest Nanotechnologies are acknowledged for their kind supply of single-walled carbon nanotubes. The Yale Institute for Nanoscience and Quantum Engineering (YINQE) and NSF MRSEC DMR 1119826 (CRISP) provided facility support.

Supporting Information Available: The Supporting Information is available free of charge on the ACS Publications website at DOI: 10.1021/acsnano.5b03578.

Additional characterization of active materials and ultrathin SSLbL electrodes includes Raman spectra, sheet conductance measurements, transmittance, microscopy and electrochemical data. (PDF)

REFERENCES AND NOTES

1. Rogers, J. A.; Someya, T.; Huang, Y. Materials and Mechanics for Stretchable Electronics. *Science* **2010**, *327*, 1603–1607.
2. Wager, J. F. Transparent Electronics. *Science* **2003**, *300*, 1245–1246.
3. Zheng, H.; Li, J.; Song, X.; Liu, G.; Battaglia, V. S. A Comprehensive Understanding of Electrode Thickness Effects on the Electrochemical Performances of Li-Ion Battery Cathodes. *Electrochim. Acta* **2012**, *71*, 258–265.
4. Zhao, R.; Liu, J.; Gu, J. The Effects of Electrode Thickness on the Electrochemical and Thermal Characteristics of Lithium Ion Battery. *Appl. Energy* **2015**, *139*, 220–229.
5. Evanoff, K.; Khan, J.; Balandin, A. A.; Magasinski, A.; Ready, W. J.; Fuller, T. F.; Yushin, G. Towards Ultrathick Battery Electrodes: Aligned Carbon Nanotube-Enabled Architecture. *Adv. Mater.* **2012**, *24*, 533–537.
6. Yang, Y.; Jeong, S.; Hu, L.; Wu, H.; Lee, S. W.; Cui, Y. Transparent Lithium-Ion Batteries. *Proc. Natl. Acad. Sci. U. S. A.* **2011**, *108*, 13013–13018.
7. Chen, T.; Xue, Y.; Roy, A. K.; Dai, L. Transparent and Stretchable Based on Wrinkled Graphene Electrodes. *ACS Nano* **2014**, *8*, 1039–1046.
8. Chen, T.; Peng, H.; Durstock, M.; Dai, L. High-Performance Transparent and Stretchable All-Solid Supercapacitors Based on Highly Aligned Carbon Nanotube Sheets. *Sci. Rep.* **2014**, *4*, 3612.
9. Jung, H. Y.; Karimi, M. B.; Hahm, M. G.; Ajayan, P. M.; Jung, Y. J. Transparent, Flexible Supercapacitors from Nano-Engineered Carbon Films. *Sci. Rep.* **2012**, *2*, 773.
10. Sorel, S.; Khan, U.; Coleman, J. N. Flexible, Transparent Dielectric Capacitors with Nanostructured Electrodes. *Appl. Phys. Lett.* **2012**, *101*, 103106.
11. Decher, G. Fuzzy Nanoassemblies: Toward Layered Polymeric Multicomposites. *Science* **1997**, *277*, 1232–1237.
12. Hammond, P. T. Engineering Materials Layer-by-Layer: Challenges and Opportunities in Multilayer Assembly. *AIChE J.* **2011**, *57*, 2928–2940.
13. Ariga, K.; Hill, J. P.; Ji, Q. Layer-by-Layer Assembly as a Versatile Bottom-up Nanofabrication Technique for Exploratory Research and Realistic Application. *Phys. Chem. Chem. Phys.* **2007**, *9*, 2319–2340.
14. Richardson, J. J.; Bjornmalm, M.; Caruso, F. Technology-Driven Layer-by-Layer Assembly of Nanofilms. *Science* **2015**, *348*, aaa2491.
15. Nam, K. T.; Kim, D.-W.; Yoo, P. J.; Chiang, C.-Y.; Meethong, N.; Hammond, P. T.; Chiang, Y.-M.; Belcher, A. M. Virus-Enabled Synthesis and Assembly of Nanowires for Lithium Ion Battery Electrodes. *Science* **2006**, *312*, 885–888.
16. Shao, L.; Jeon, J.-W.; Lutkenhaus, J. L. Polyaniline/Vanadium Pentoxide Layer-by-Layer Electrodes for Energy Storage. *Chem. Mater.* **2012**, *24*, 181–189.
17. Hyder, M. N.; Gallant, B. M.; Shah, N. J.; Shao-Horn, Y.; Hammond, P. T. Synthesis of Highly Stable Sub-8 Nm TiO_2 Nanoparticles and Their Multilayer Electrodes of TiO_2/MWNT for Electrochemical Applications. *Nano Lett.* **2013**, *13*, 4610–4619.
18. Hyder, M. N.; Lee, S. W.; Cebeci, F. Ç.; Schmidt, D. J.; Shao-Horn, Y.; Hammond, P. T. Layer-by-Layer Assembled Polyaniline Nanofiber/Multiwall Carbon Nanotube Thin Film Electrodes for High-Power and High-Energy Storage Applications. *ACS Nano* **2011**, *5*, 8552–8561.
19. Hyder, N.; Kavian, R.; Sultana, Z.; Saetia, K.; Chen, P.; Lee, S. W.; Shao-Horn, Y.; Hammond, P. T. Vacuum-Assisted Layer-by-Layer Nanocomposites for Self-Standing 3D Mesoporous Electrodes. *Chem. Mater.* **2014**, *26*, 5310–5318.
20. Lee, S. W.; Kim, B.-S.; Chen, S.; Shao-Horn, Y.; Hammond, P. T. Layer-by-Layer Assembly of All Carbon Nanotube Ultrathin Films for Electrochemical Applications. *J. Am. Chem. Soc.* **2009**, *131*, 671–679.
21. Lee, S. W.; Yabuuchi, N.; Gallant, B. M.; Chen, S.; Kim, B.-S.; Hammond, P. T.; Shao-Horn, Y. High-Power Lithium Batteries from Functionalized Carbon-Nanotube Electrodes. *Nat. Nanotechnol.* **2010**, *5*, 531–537.
22. Kim, S. Y.; Hong, J.; Kavian, R.; Lee, S. W.; Hyder, M. N.; Shao-Horn, Y.; Hammond, P. T. Rapid Fabrication of Thick Spray-Layer-by-Layer Carbon Nanotube Electrodes for High Power and Energy Devices. *Energy Environ. Sci.* **2013**, *6*, 888–897.
23. Gallant, B. M.; Lee, S. W.; Kawaguchi, T.; Hammond, P. T.; Shao-Horn, Y. Electrochemical Performance of Thin-Film Functionalized Carbon Nanotube Electrodes in Nonaqueous Cells. *J. Electrochem. Soc.* **2014**, *161*, A1625–A1633.
24. Lee, S. W.; Gallant, B. M.; Lee, Y.; Yoshida, N.; Kim, D. Y.; Yamada, Y.; Noda, S.; Yamada, A.; Shao-Horn, Y. Self-Standing Positive Electrodes of Oxidized Few-Walled Carbon Nanotubes for Light-Weight and High-Power Lithium Batteries. *Energy Environ. Sci.* **2012**, *5*, 5437–5444.
25. Lee, S. W.; Kim, J.; Chen, S.; Hammond, P. T.; Shao-Horn, Y. Carbon Nanotube/Manganese Oxide Ultrathin Film Electrodes for Electrochemical Capacitors. *ACS Nano* **2010**, *4*, 3889–3896.
26. Taylor, A. D.; Michel, M.; Sekol, R. C.; Kizuka, J. M.; Kotov, N. A.; Thompson, L. T. Fuel Cell Membrane Electrode Assemblies Fabricated by Layer-by-Layer Electrostatic Self-Assembly Techniques. *Adv. Funct. Mater.* **2008**, *18*, 3003–3009.
27. Daiko, Y.; Katagiri, K.; Yazawa, T.; Matsuda, A. Thickness Dependences of Proton Conductivity for Ultrathin Nafion Multilayers Prepared *via* Layer-by-Layer Assembly. *Solid State Ionics* **2010**, *181*, 197–200.
28. Michel, M.; Ettingshausen, F.; Scheiba, F.; Wolz, A.; Roth, C. Using Layer-by-Layer Assembly of Polyaniline Fibers in the Fast Preparation of High Performance Fuel Cell

Nanostructured Membrane Electrodes. *Phys. Chem. Chem. Phys.* **2008**, *10*, 3796–3801.
29. Wolz, A.; Zils, S.; Michel, M.; Roth, C. Structured Multilayered Electrodes of Proton/Electron Conducting Polymer for Polymer Electrolyte Membrane Fuel Cells Assembled by Spray Coating. *J. Power Sources* **2010**, *195*, 8162–8167.
30. Michel, M.; Taylor, A.; Sekol, R.; Podsiadlo, P.; Ho, P.; Kotov, N.; Thompson, L. High-Performance Nanostructured Membrane Electrode Assemblies for Fuel Cells Made by Layer-By-Layer Assembly of Carbon Nanocolloids. *Adv. Mater.* **2007**, *19*, 3859–3864.
31. Ren, H.; Pyo, S.; Lee, J.-I.; Park, T.-J.; Gittleson, F. S.; Leung, F. C. C.; Kim, J.; Taylor, A. D.; Lee, H.-S.; Chae, J. A High Power Density Miniaturized Microbial Fuel Cell Having Carbon Nanotube Anodes. *J. Power Sources* **2015**, *273*, 823–830.
32. Shim, B. S.; Tang, Z.; Morabito, M. P.; Agarwal, A.; Hong, H.; Kotov, N. A. Integration of Conductivity, Transparency, and Mechanical Strength into Highly Homogeneous Layer-by-Layer Composites of Single-Walled Carbon Nanotubes for Optoelectronics. *Chem. Mater.* **2007**, *19*, 5467–5474.
33. Shim, B. S.; Zhu, J.; Jan, E.; Critchley, K.; Kotov, N. A. Transparent Conductors from Layer-by-Layer Assembled SWNT Films: Importance of Mechanical Properties and a New Figure of Merit. *ACS Nano* **2010**, *4*, 3725–3734.
34. Hong, T.-K.; Lee, D. W.; Choi, H. J.; Shin, H. S.; Kim, B.-S. Transparent, Flexible Conducting Hybrid Multilayer Thin Films of Multiwalled Carbon Nanotubes with Graphene Nanosheets. *ACS Nano* **2010**, *4*, 3861–3868.
35. Loh, K. J.; Kim, J.; Lynch, J. P.; Kam, N. W. S.; Kotov, N. A. Multifunctional Layer-by-Layer Carbon Nanotube–Polyelectrolyte Thin Films for Strain and Corrosion Sensing. *Smart Mater. Struct.* **2007**, *16*, 429–438.
36. Lutkenhaus, J. L.; Hammond, P. T. Electrochemically Enabled Polyelectrolyte Multilayer Devices: From Fuel Cells to Sensors. *Soft Matter* **2007**, *3*, 804–816.
37. Srivastava, S.; Kotov, N. A. Composite Layer-by-Layer (LBL) Assembly with Inorganic Nanoparticles and Nanowires. *Acc. Chem. Res.* **2008**, *41*, 1831–1841.
38. Gittleson, F. S.; Kohn, D. J.; Li, X.; Taylor, A. D. Improving the Assembly Speed, Quality, and Tunability of Thin Conductive Multilayers. *ACS Nano* **2012**, *6*, 3703–3711.
39. Xiang, Y.; Lu, S.; Jiang, S. P. Layer-by-Layer Self-Assembly in the Development of Electrochemical Energy Conversion and Storage Devices from Fuel Cells to Supercapacitors. *Chem. Soc. Rev.* **2012**, *41*, 7291–7321.
40. Shao, L.; Jeon, J.; Lutkenhaus, J. L. Porous Polyaniline Nanofiber/Vanadium Pentoxide Layer-by-Layer Electrodes for Energy Storage. *J. Mater. Chem. A* **2013**, *1*, 7648–7656.
41. Shao, L.; Jeon, J.-W.; Lutkenhaus, J. L. Polyaniline Nanofiber/Vanadium Pentoxide Sprayed Layer-by-Layer Electrodes for Energy Storage. *J. Mater. Chem. A* **2014**, *2*, 14421–14428.
42. Gomes, W. J. A. S.; Araújo, D. M.; Carvalho, A. J. F.; Campana-Filho, S. P.; Huguenin, F. High Lithium Ion Electroinsertion Rate into Self-Assembled Films Formed from TiO_2. *J. Phys. Chem. C* **2013**, *117*, 16774–16782.
43. Landi, B. J.; Ganter, M. J.; Cress, C. D.; DiLeo, R. A.; Raffaelle, R. P. Carbon Nanotubes for Lithium Ion Batteries. *Energy Environ. Sci.* **2009**, *2*, 638–654.
44. Landi, B. J.; Cress, C. D.; Raffaelle, R. P. High Energy Density Lithium-Ion Batteries with Carbon Nanotube Anodes. *J. Mater. Res.* **2010**, *25*, 1636–1644.
45. Landi, B. J.; Ganter, M. J.; Schauerman, C. M.; Cress, C. D.; Raffaelle, R. P. Lithium Ion Capacity of Single Wall Carbon Nanotube Paper Electrodes. *J. Phys. Chem. C* **2008**, *112*, 7509–7515.
46. Li, X.; Gittleson, F.; Carmo, M.; Sekol, R. C.; Taylor, A. D. Scalable Fabrication of Multifunctional Freestanding Carbon Nanotube/Polymer Composite Thin Films for Energy Conversion. *ACS Nano* **2012**, *6*, 1347–1356.
47. Shimoda, H.; Gao, B.; Tang, X.; Kleinhammes, A.; Fleming, L.; Wu, Y.; Zhou, O. Lithium Intercalation into Opened Single-Wall Carbon Nanotubes: Storage Capacity and Electronic Properties. *Phys. Rev. Lett.* **2001**, *88*, 015502.
48. Claye, A. S.; Fischer, J. E.; Huffman, C. B.; Rinzler, A. G.; Smalley, R. E. Solid-State Electrochemistry of the Li Single Wall Carbon Nanotube System. *J. Electrochem. Soc.* **2000**, *147*, 2845–2852.
49. Zurita-Gotor, M.; Gittleson, F. S.; Taylor, A. D.; Blawzdziewicz, J. Stratified Rod Network Model of Electrical Conductance in Ultrathin Polymer–Carbon Nanotube Multilayers. *Phys. Rev. B: Condens. Matter Mater. Phys.* **2013**, *87*, 195449.
50. Hu, L.; Hecht, D. S.; Gruner, G. Carbon Nanotube Thin Films: Fabrication, Properties, and Applications. *Chem. Rev.* **2010**, *110*, 5790–5844.
51. Park, Y. T.; Ham, A. Y.; Grunlan, J. C. High Electrical Conductivity and Transparency in Deoxycholate-Stabilized Carbon Nanotube Thin Films. *J. Phys. Chem. C* **2010**, *114*, 6325–6333.
52. Bressers, P. M.; Meulenkamp, E. A. The Electrochromic Behavior of Indium Tin Oxide in Propylene Carbonate Solutions. *J. Electrochem. Soc.* **1998**, *145*, 2225–2230.
53. Kulkarni, G. U.; Kiruthika, S.; Gupta, R.; Rao, K. Towards Low Cost Materials and Methods for Transparent Electrodes. *Curr. Opin. Chem. Eng.* **2015**, *8*, 60–68.
54. Whitehead, A. H.; Schreiber, M. Current Collectors for Positive Electrodes of Lithium-Based Batteries. *J. Electrochem. Soc.* **2005**, *152*, A2105.
55. Xu, K. Electrolytes and Interphases in Li-Ion Batteries and Beyond. *Chem. Rev.* **2014**, *114*, 11503–11618.
56. Park, Y. T.; Ham, A. Y.; Grunlan, J. C. Heating and Acid Doping Thin Film Carbon Nanotube Assemblies for High Transparency and Low Sheet Resistance. *J. Mater. Chem.* **2011**, *21*, 363–368.
57. Delmas, C.; Cognacauradou, H.; Cocciantelli, J.; Menetrier, M.; Doumerc, J. The $Li_xV_2O_5$ System: An Overview of the Structure Modifications Induced by the Lithium Intercalation. *Solid State Ionics* **1994**, *69*, 257–264.
58. Chan, C. K.; Peng, H.; Twesten, R. D.; Jarausch, K.; Zhang, X. F.; Cui, Y. Fast, Completely Reversible Li Insertion in Vanadium Pentoxide Nanoribbons. *Nano Lett.* **2007**, *7*, 490–495.
59. Wang, Y.; Takahashi, K.; Lee, K. H.; Cao, G. Z. Nanostructured Vanadium Oxide Electrodes for Enhanced Lithium-Ion Intercalation. *Adv. Funct. Mater.* **2006**, *16*, 1133–1144.
60. Li, X.; Li, W.; Ma, H.; Chen, J. Electrochemical Lithium Intercalation/Deintercalation of Single-Crystalline V_2O_5 Nanowires. *J. Electrochem. Soc.* **2007**, *154*, A39–A42.
61. Liu, Y.; Clark, M.; Zhang, Q.; Yu, D.; Liu, D.; Liu, J.; Cao, G. V_2O_5 Nano-Electrodes with High Power and Energy Densities for Thin Film Li-Ion Batteries. *Adv. Energy Mater.* **2011**, *1*, 194–202.
62. Livage, J. Synthesis of Polyoxovanadates *via* "Chimie Douce". *Coord. Chem. Rev.* **1998**, *178–180*, 999–1018.
63. Livage, J. Vanadium Pentoxide Gels. *Chem. Mater.* **1991**, *3*, 578–593.
64. Gittleson, F. S.; Hwang, J.; Sekol, R. C.; Taylor, A. D. Polymer Coating of Vanadium Oxide Nanowires to Improve Cathodic Capacity in Lithium Batteries. *J. Mater. Chem. A* **2013**, *1*, 7979–7984.
65. Beattie, I.; Gilson, T. Oxide Phonon Spectra. *J. Chem. Soc. A* **1969**, 2322–2327.
66. Zhou, F.; Zhao, X.; Yuan, C.; Li, L. Vanadium Pentoxide Nanowires: Hydrothermal Synthesis, Formation Mechanism, and Phase Control Parameters. *Cryst. Growth Des.* **2008**, *8*, 723–727.
67. Avansi, W., Jr.; Ribeiro, C.; Leite, E. R.; Mastelaro, V. R. Vanadium Pentoxide Nanostructures: An Effective Control of Morphology and Crystal Structure in Hydrothermal Conditions. *Cryst. Growth Des.* **2009**, *9*, 3626–3631.
68. Magasinski, A.; Zdyrko, B.; Kovalenko, I.; Hertzberg, B.; Burtovyy, R.; Huebner, C. F.; Fuller, T. F.; Luzinov, I.; Yushin, G. Toward Efficient Binders for Li-Ion Battery Si-Based Anodes: Polyacrylic Acid. *ACS Appl. Mater. Interfaces* **2010**, *2*, 3004–3010.
69. Delongchamp, D. M.; Hammond, P. T. Fast Ion Conduction in Layer-by-Layer Polymer Films. *Chem. Mater.* **2003**, *15*, 1165–1173.
70. DeLongchamp, D. M.; Hammond, P. T. Highly Ion Conductive Poly(Ethylene Oxide)-Based Solid Polymer Electrolytes

from Hydrogen Bonding Layer-by-Layer Assembly. *Langmuir* **2004**, *20*, 5403–5411.
71. Lutkenhaus, J. L.; Mcennis, K.; Hammond, P. T. Tuning the Glass Transition of and Ion Transport within Hydrogen-Bonded Layer-by-Layer Assemblies. *Macromolecules* **2007**, *40*, 8367–8373.
72. Vigolo, B.; Zakri, C.; Nallet, F.; Livage, J.; Coulon, C. Detailed Study of Diluted V_2O_5 Suspensions. *Langmuir* **2002**, *18*, 9121–9132.
73. Muster, B. J.; Kim, G. T.; Krstic, V.; Park, J. G.; Park, Y. W.; Roth, S. Electrical Transport Through Individual Vanadium Pentoxide Nanowires. *Adv. Mater.* **2000**, *12*, 420–424.
74. Costa, C.; Pinheiro, C.; Henriques, I.; Laia, C. A. T. Electrochromic Properties of Inkjet Printed Vanadium Oxide Gel on Flexible Polyethylene Terephthalate/Indium Tin Oxide Electrodes. *ACS Appl. Mater. Interfaces* **2012**, *4*, 5266–5275.
75. Cogan, S. F.; Nguyen, N. M.; Perrotti, S. J.; Rauh, R. D. Optical Properties of Electrochromic Vanadium Pentoxide. *J. Appl. Phys.* **1989**, *66*, 1333–1337.